Electronic Supplementary Material (ESI) for Inorganic Chemistry Frontiers.
This journal is © the Partner Organisations 2024

Supporting Information

A dual-heteroatom–lanthanide cluster-embedded polyoxotungstate for sequential fluorescence detection of Fe^{3+} and pyrophosphate

Siyu Zhang,‡[a,b] Tiantian Gong,‡[b] Chenyun Liu,[a,b] Qiuyu Wang,[b] Fuxiu Chen,[b] Jiancai Liu,*[a,b] Lijuan Chen,*[b] Junwei Zhao*[a,b]

[a]School of Energy Science and Technology, Henan University, Zhengzhou, Henan 450046, People's Republic of China. E-mail: liujiancai@henu.edu.cn
[b]Henan Key Laboratory of Polyoxometalate Chemistry, College of Chemistry and Chemical Engineering, Henan University, Kaifeng, Henan 475004, People's Republic of China. E-mail: ljchen@henu.edu.cn, zhaojunwei@henu.edu.cn

Materials and physical measurements

All chemicals were commercially available and used without further purification. C, H and N elemental analyses were performed on a Perkin–Elmer 2400–II CHNS analyzer. Inductively coupled plasma-atomic emission spectroscopy (ICP−AES) analyses were performed on a Perkin–Elmer Optima 2000DV ICP−AES spectrometer. Fourier Transform Infrared (FT-IR) spectrum was received from solid samples palletized with KBr on BRUKER TENSOR II FT-IR spectra spectrometer between 4000–400 cm^{-1}. Thermogravimetric (TG) analysis was measured on a Bruker Tensor–II TGA instrument under the N_2 atmosphere with a heating rate of 10 °C/min in the temperature range of 25–1000 °C. Powder X-ray diffraction (PXRD) data were recorded on a Bruker D8 ADVANCE apparatus using Cu *Kα* radiation (*λ* = 1.54056 Å) in a scan range (2*ϑ*) of 5–50° at 293 K. Electrospray ionization mass spectrometry (ESI-MS) tests were performed on an AB SCIEX Triple TOF 4600 spectrometer operating in negative-ion mode and the data was analyzed using the Peakview 2.0 software provided. UV-vis spectra were recorded on an UV-6100 double beam spectrophotometer in the range of 190–500 nm in aqueous solution. Photoluminescence (PL) spectra were investigated by Edinburgh FLS 980 Analytical Instrument apparatus with 450 W Xe-lamp as excitation source, and the PL decay lifetime curves were monitored by using the μF900H high-energy microsecond flash lamp.

X-ray crystallography

The diffraction data of **1** were collected on a Bruker D8 Venture Photon II diffractometer equipped with CCD two-dimensional detector using monochromated Mo *Kα* radiation (*λ* = 0.71073 Å) at 150 K. Routine Lorentz and polarization corrections were applied and a multi-scan absorption correction was utilized with the SADABS program. The structures were solved using direct methods, and refined on F^2 by full-matrix least-squares method with the assistance of SHELXTL–97 program. All H atoms coordinated with N and C atoms were generated geometrically and refined isotropically as a riding model using the default SHELXTL parameters. No H atoms associated with water molecules are located from the difference Fourier map. All non-H atoms are refined anisotropically. Besides, one $[H_2N(CH_3)_2]^+$ cation, one Na^+ cation and 25 lattice water molecules were directly added into the molecular formula of **1** based on charge balance requirement, elemental and TG analyses. The crystallographic data and structure refinements for **1** are listed in Table S1. Crystallographic data and structure refinements for **1** reported in this paper have been deposited in the Cambridge Crystallographic Data Centre with CCDC 2335445 for **1**. These data can be obtained free of charge from the Cambridge Crystallographic Data Centre via www.ccdc.cam.ac.uk/data_ request/cif.

Synthesis of $[H_8BTHMMAP]_{1.5}[H_2N(CH_3)_2]_4Na_3H[Eu_2Bi_3(Hpdca)_3(H_2O)_3Te_2W_3O_{14}][(W_5O_{18})(B\text{-}\alpha\text{-}BiW_9O_{33})_2]\cdot 44H_2O$ (1)

$Na_2WO_4\cdot 2H_2O$ (3.401 g, 10.311 mmol), K_2TeO_3 (0.130 g, 0.512 mmol), dimethylamine hydrochloride (0.705 g, 8.645 mmol), 1,3-bis[tris(hydroxymethyl)methylamino]propane ($H_6BTHMMAP$, 0.200 g, 0.712 mmol), 2-pyridinecarboxylic acid (0.202 g, 1.641 mmol) were dissolved in 30 mL distilled water under stirring. Then $Bi(NO_3)_3\cdot 5H_2O$ (0.201 g, 0.412 mmol) was dissolved in 1 mL hydrochloric acid (6 M) and added drop by drop to the above solution, and the pH of the solution was adjusted to 6.0 by 6 M HCl. Subsequently, $Eu(NO_3)_3\cdot 6H_2O$ (0.400 g, 0.897 mmol) was added to the solution and the final pH of the solution was kept about 5.30 using 4 M NaOH. The solution was heated at 90 °C for 2 h, then cooled to room temperature and filtered. Slow evaporation of the filtrate led to colorless block

crystals after about ten days. Yield: 0.22 g. Elemental analysis: calcd (%) for C, 5.18; H, 1.88; N, 1.42; W, 48.53. Found (%) for C, 5.30; H, 1.77; N, 1.53; W, 48.41.

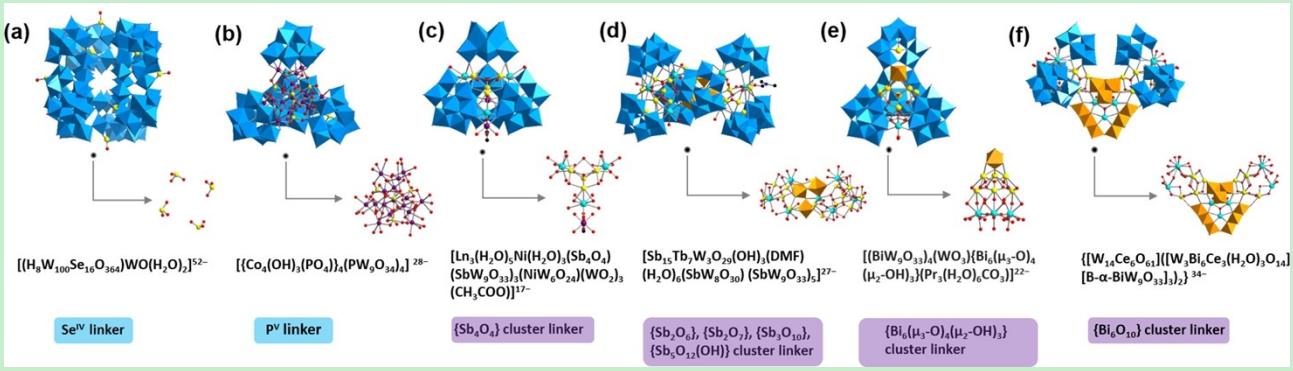

Fig. S1 Structures of some representative dual-HA-directed HPOTs, where HAs work as discrete linkers or cluster linkers.

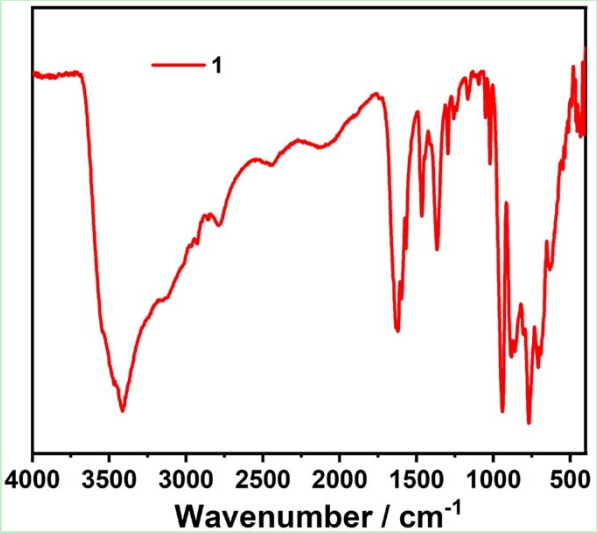

Fig. S2 The IR spectrum of **1**.

IR spectrum of **1** was recorded on a Perkin-Elmer FT-IR spectrophotometer in the range of 4000–400 cm^{-1} by palletization with KBr. In the low wavenumber (ν < 1000 cm^{-1}) region, several characteristic vibrations appearing at 941; 882, 861; 692, 632; and 547 cm^{-1} are respectively ascribed to the W–O_t, corner-sharing W–O_b, edge-sharing W–O_c and Bi–O vibrations.[1] The band at 711 cm^{-1} is assigned to Te–O_a vibrations. In the high wavenumber (ν > 1000 cm^{-1}) region, the weak peaks at 1051 and 1022 cm^{-1} can be assigned to the $\delta_s(CH_3)$ vibration in H_8BTHMMAP.[2] The bands located at 1367, 1466 and 1621 with a splitting peak at 1633 cm^{-1} correspond to the COO^- stretching vibrations of the Hpdca ligand.[3] In addition, the bands in the range 1650–1550 cm^{-1} are ascribed to the C=C and C=N stretching vibrations of Hpdca ring. The signal at 2806 cm^{-1} can be assigned as the C−H stretching vibrations, illustrating the presence of protonated dimethylamine cations. The broad vibration bands situated in the range of 3503–3306 cm^{-1} and the peak at about 1630–1621 cm^{-1} are response for water molecules.

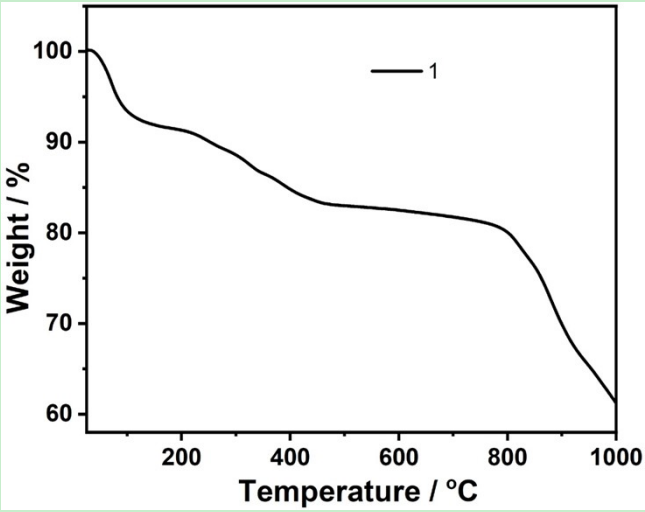

Fig. S3 The TG curve of **1**.

The thermal-stability measurement of **1** was performed under N_2 atmosphere with a heating speed of 10 °C/min from 25 to 1000 °C. The TG curve of **1** displays a three-step weight loss. The first weight loss of 8.36% (calcd. 8.05%) from 25 to 170 °C belongs to the liberation of 44 lattice water molecules. The second weight loss of 10.71% (calcd. 11.16%) occurs from 170 to 770 °C, which correspond to the loss of 3 coordination water molecules, 4 dimethylamine molecules, 1.5 [H_6BTHMMAP] molecules, 3 Hpdca ligands and dehydration of 8 protons. As temperatures rise to 1000 °C, the polyanion structure of **1** gradually disintegrates.

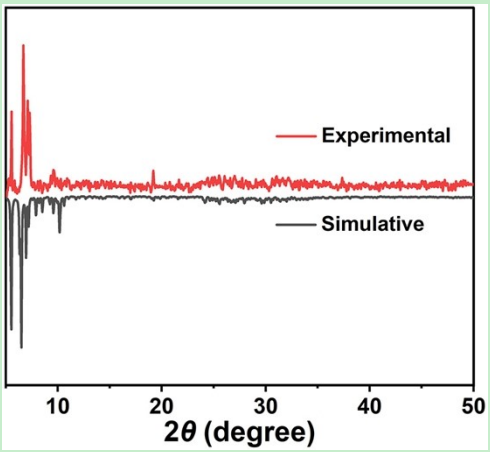

Fig. S4 Comparison of the simulative and experimental PXRD patterns of **1**.

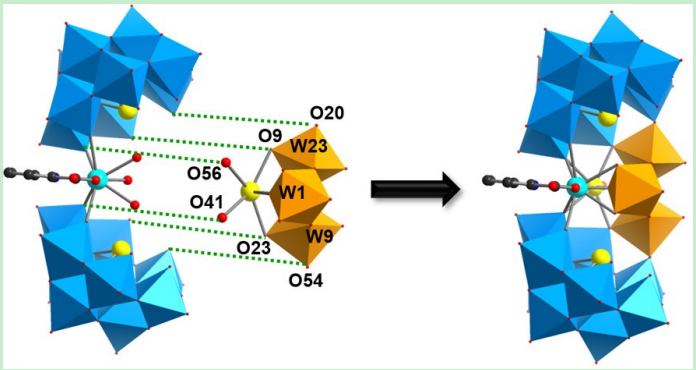

Fig. S5 Highlighting the bridging O atoms in connecting the dimeric midbody and $[BiW_3(H_2O)O_{11}]^-$ moiety.

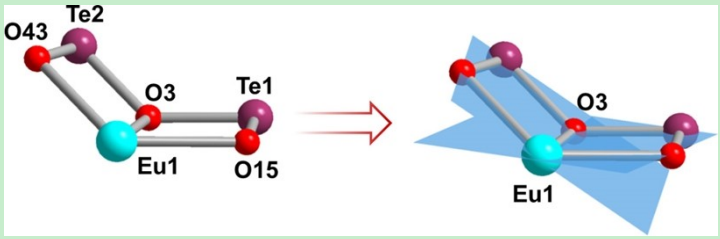

Fig. S6 The $[EuTe_2O_3]^{5+}$ cluster showing a folded quadrangle-shaped motif along ''Eu1–O3'' line.

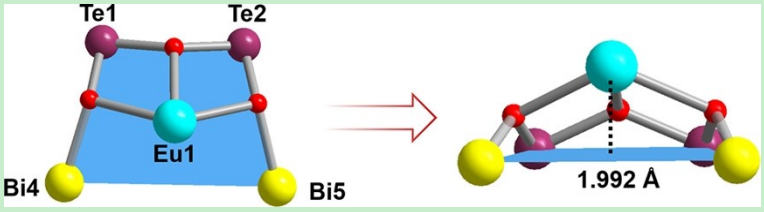

Fig. S7 The almost coplanar arrangement of two Te^{IV} and two Bi^{III} atoms with $Eu1^{3+}$ ion located above the plane with a distance of 1.992 Å.

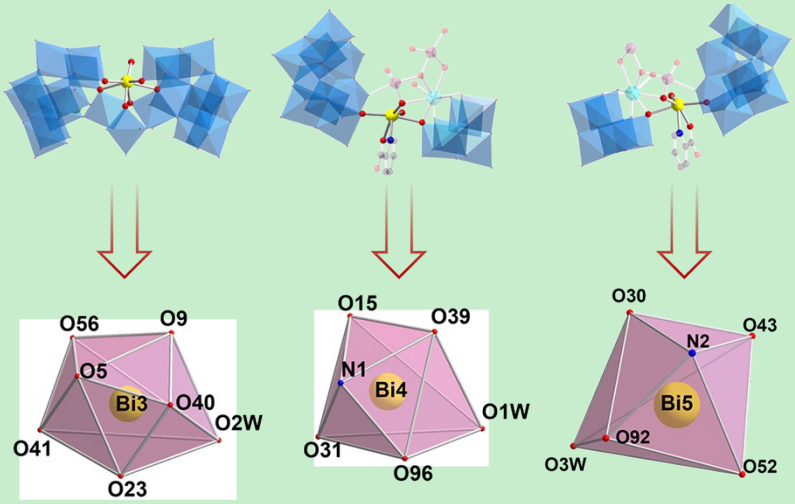

Fig. S8 Coordination environments of $Bi3^{III}$–$Bi5^{III}$ atoms.

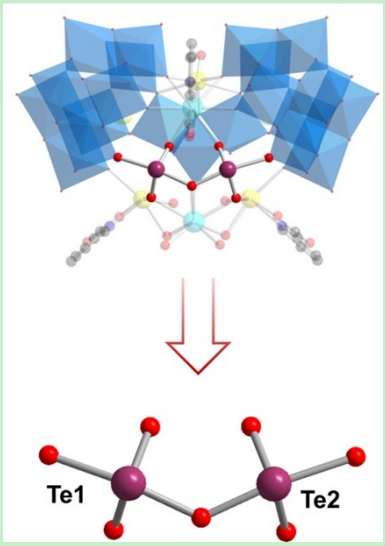

Fig. S9 Coordination environments of $Te1^{IV}$ and $Te2^{IV}$ atoms.

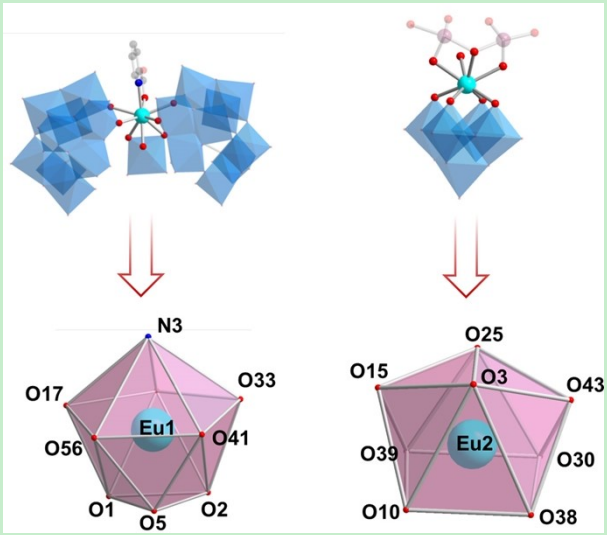

Fig. S10 Coordination geometries of $Eu1^{3+}$ and $Eu2^{3+}$ ions.

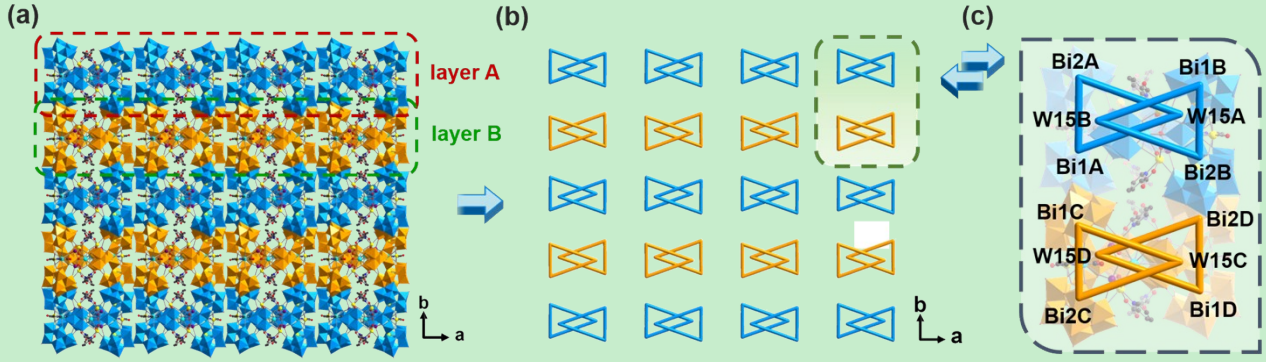

Fig. S11 (a) The stacking structure of **1a**. (b) The simplified diagram of stacking structure of **1a**. (c) The repeating unit in each layer. Symmetry code: A (2 – x, 1.5 + y, 1.5 – z), B (2 + x, 2.5 – y, 1.5 + z), C (2 – x, 2 – y, 2 – z), D (2 + x, 1 + y, 1 + z).

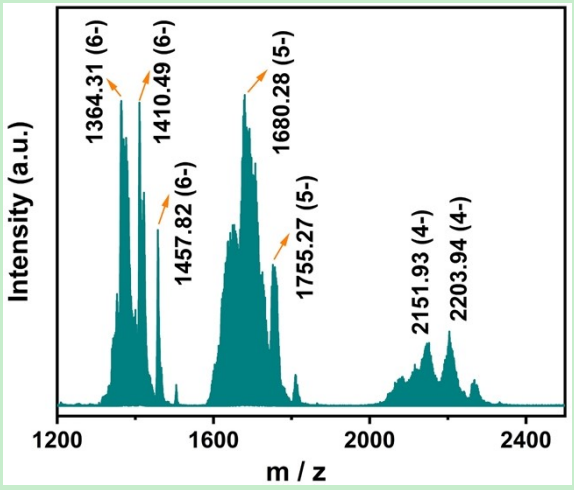

Fig. S12 The ESI-MS spectrum of **1** in aqueous solution.

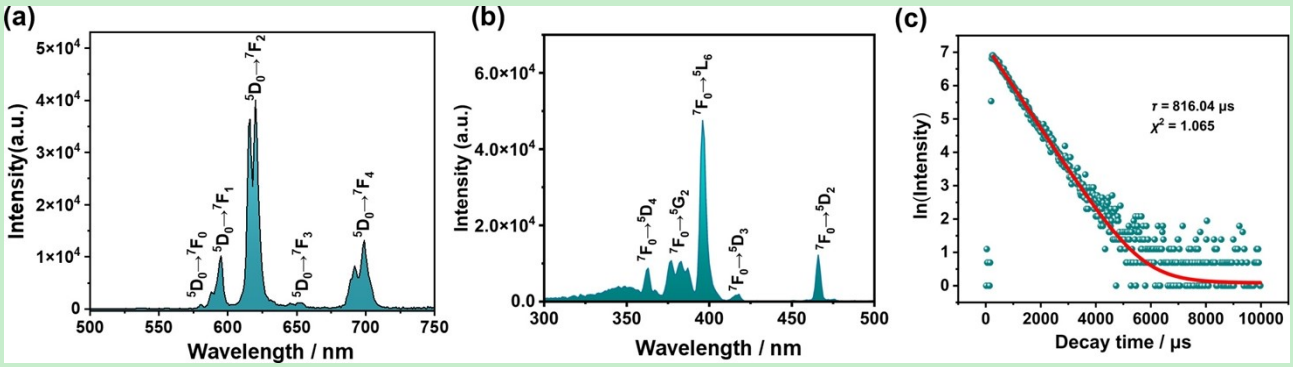

Fig. S13 (a) The emission spectrum of **1** in aqueous solution (λ_{ex} = 397 nm). (b) The excitation spectrum of **1** in aqueous solution (λ_{em} = 620 nm). (c) The luminescence decay curve of **1** by monitoring the emission at 620 nm in aqueous solution.

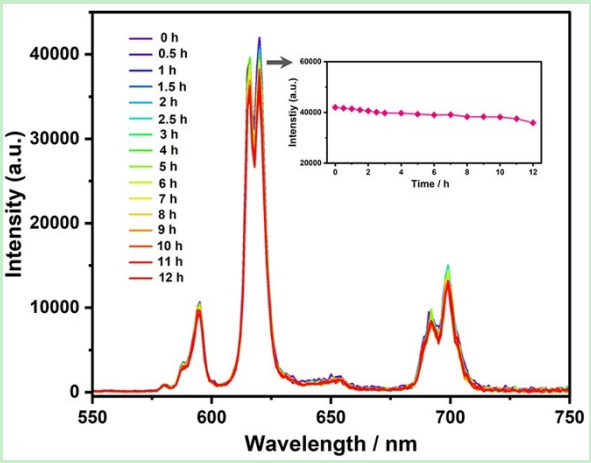

Fig. S14 Time-dependent PL emission of **1** in water.

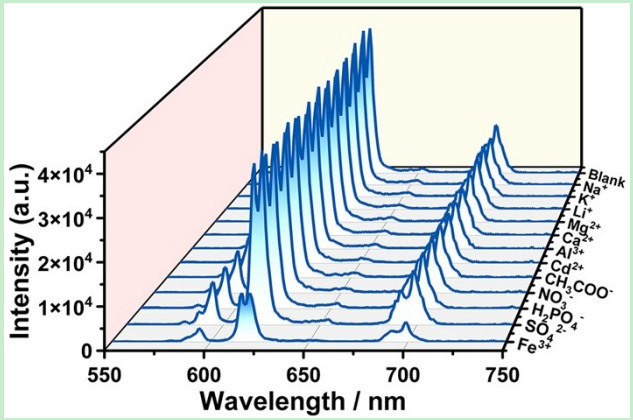

Fig. S15 Fluorescence responses of the **1**-based sensor towards Fe^{3+} and other ions.

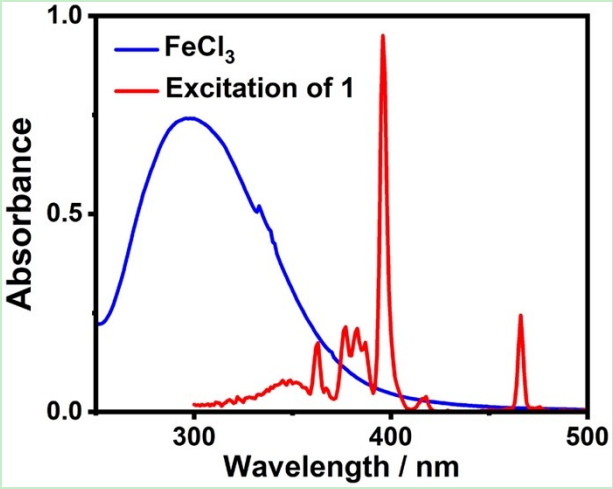

Fig. S16 Overlap between the UV–vis absorption spectra of $FeCl_3$ and the excitation spectra of **1**.

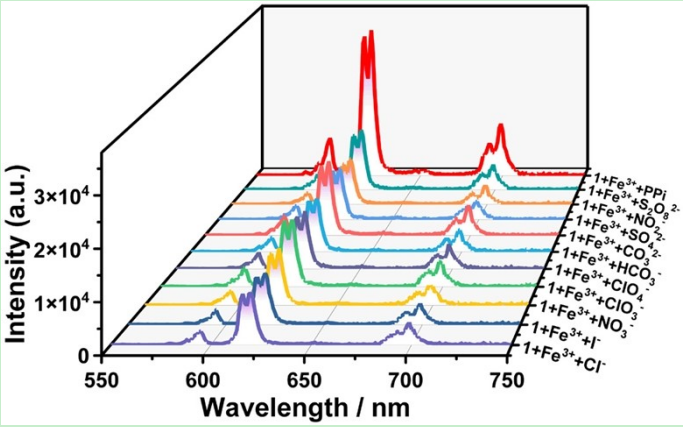

Fig. S17 Fluorescence responses of the Fe^{3+}-quenched system with different anions.

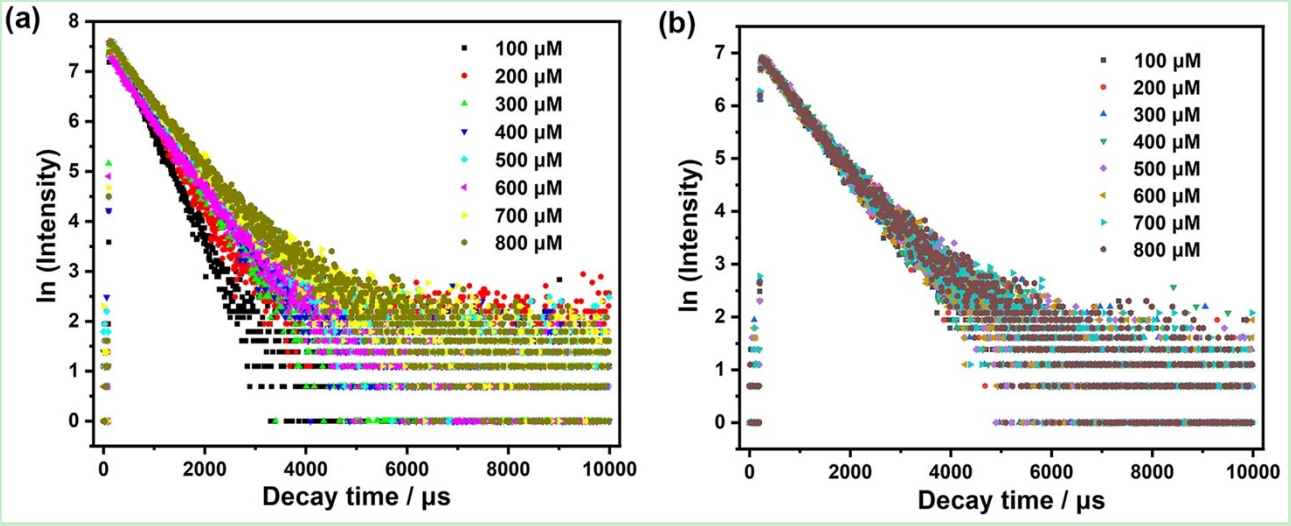

Fig. S18 (a) Lifetime decay curves of the Fe^{3+}-quenched system under different concentrations of PPi. (b) Lifetime decay curves of **1** under different concentrations of PPi.

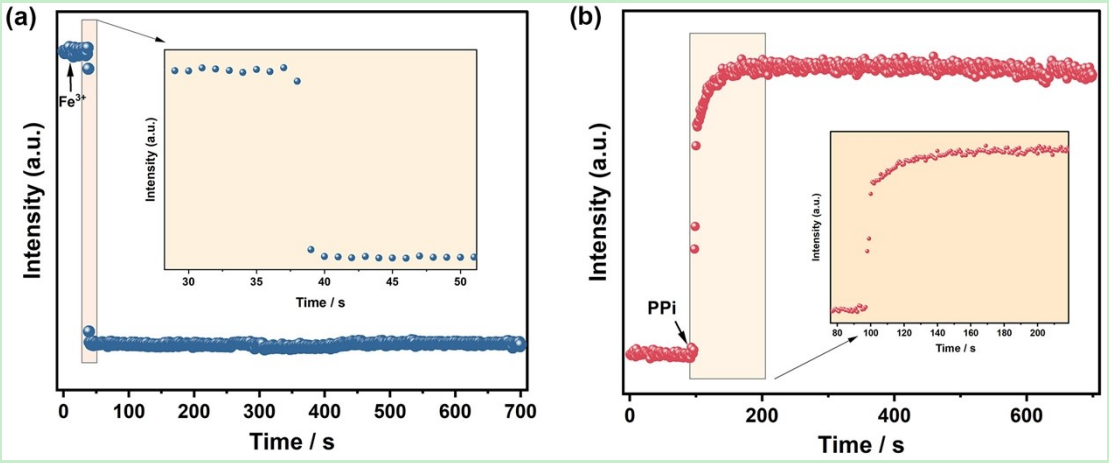

Fig. S19 (a) Time scan of the PL response of **1** towards the addition of Fe^{3+} (400 μM). (b) Time scan of the PL response of Fe^{3+}-quenched system towards the addition of PPi (800 μM).

Table S1. X-ray diffraction crystallographic data and structure refinements for **1**.

	1
Empirical formula	$C_{42.50}H_{184}Bi_5Eu_2N_{10}Na_3O_{160}Te_2W_{26}$
Formula weight	9849.09
Temperature	150(2) K
Wavelength	0.71073 A
Crystal system	Monoclinic
space group	*P*2(1)/c
a / Å	22.7494(5)
b / Å	29.3558(5)
c / Å	27.6875(7)
α / °	90
β / °	100.7660(10)
γ / °	90
V / Å^3	18165.0(7)
Z	4
ρ_{calc} / g cm^{-3}	3.601
μ / mm^{-1}	22.330
F(000)	17564
Crystal size / mm^3	0.18 x 0.15 x 0.10
Radiation	Mo *Kα* (*λ* = 0.71073)
2*ϑ* range for data collection/°	1.89 to 25.10
Index ranges	$-27 \le h \le 27$ $-33 \le k \le 35$ $-33 \le l \le 33$
Reflections collected	233821
Data/restrains/parameters	32271 / 13 / 1843
Goodness-of-fit on F^2	1.047
R_1, wR_2 ($I > 2\sigma(I)$)	R_1 = 0.0390, wR_2 = 0.0994
R_1, wR_2 (all data)	R_1 = 0.0549, wR_2 = 0.1076

Table S2. Assignment of peaks with proposed formula and charges.

z	*m/z* (obs)	*m/z* (calc)	Assignment
6–	1364.31	1364.17	$[H_2N(CH_3)_2]_2Na_3[Eu_2Bi_3(H_2O)_4Te_2W_3O_{14}][(W_5O_{18})(BiW_9O_{33})_2]^{6-}$
	1410.49	1410.88	$[H_2N(CH_3)_2]H_3Na[Eu_2Bi_3(Hpdca)_3(H_2O)_4Te_2W_3O_{14}][(W_5O_{18})(BiW_9O_{33})_2]^{6-}$
	1457.82	1457.94	$[H_8BTHMMAP][H_2N(CH_3)_2]HNa[Eu_2Bi_3(Hpdca)_3(H_2O)_4Te_2W_3O_{14}][(W_5O_{18})(BiW_9O_{33})_2]^{6-}$
5–	1680.28	1680.64	$NaH_5[Eu_2Bi_3(Hpdca)_3(H_2O)_3Te_2W_3O_{14}][(W_5O_{18})(BiW_9O_{33})_2]^{5-}$
	1755.27	1755.14	$[H_8BTHMMAP][H_2N(CH_3)_2]_2HNa[Eu_2Bi_3(Hpdca)_3(H_2O)_3Te_2W_3O_{14}][(W_5O_{18})(BiW_9O_{33})_2]^{5-}$
4–	2151.93	2151.64	$[H_2N(CH_3)_2]_4Na_2H[Eu_2Bi_3(Hpdca)_3(H_2O)_3Te_2W_3O_{14}][(W_5O_{18})(BiW_9O_{33})_2]^{4-}$
	2203.94	2204.18	$[H_8BTHMMAP][H_2N(CH_3)_2]_2Na_2H[Eu_2Bi_3(Hpdca)_3(H_2O)_4Te_2W_3O_{14}][(W_5O_{18})(BiW_9O_{33})_2]^{4-}$

Table S3. The standard deviation for the **1**-based fluorescence sensor.

	I **(fluorescence intensity of the peak at 620 nm)**	**AVG. (Average of *I*)**	**AVG. / *I***	**Standard Deviation (*s*)**
Sample 1	43265.7031		0.999	
Sample 2	43236.5859	43230.4544	1.000	8.949×10^{-4}
Sample 3	43189.0742		1.001	

According to the definition of LOD = 3*s*/*k*, bring $s = 8.949 \times 10^{-4}$ and $k = 0.00218$ into the above formula, the LOD can be calculated as 1.23 μM.

Table S4. Detection results of Fe^{3+} by **1**-based fluorescence sensor in real samples.

Sample	**Spiked (μM)**	**Measured (μM)**	**Recovery (%)**	**RSD (n = 3, %)**
tap water	40	39.68	99.19	1.82
	80	80.26	100.33	0.88
	120	120.60	100.50	0.83
lake water	40	39.60	99.00	0.55
	80	79.37	99.21	0.27
	120	120.21	100.18	0.94
Human serum	40	40.71	101.78	0.34
	80	80.24	100.30	1.23
	120	119.47	99.56	0.34

Table S5. Decay lifetimes of the **1**-based sensor under different concentrations of Fe^{3+}.

Concentration of Fe^{3+} / μM	**Decay time / μs**
Blank	816.04
50 μM	762.34
100 μM	703.51
150 μM	642.19

200 μM	566.58
250 μM	520.24
300 μM	468.98
350 μM	424.71
400 μM	400.14

Table S6. The standard deviation for the Fe^{3+}-quenched system.

	I **(fluorescence intensity of the peak at 620 nm)**	**AVG. (Average of *I*)**	**AVG. / *I***	**Standard Deviation (*s*)**
Sample 1	11159.2373	11172.4189	1.001	1.231×10^{-3}
Sample 2	11171.3379		1.000	
Sample 3	11186.6816		0.999	

According to the definition of LOD = 3*s*/*k*, bring $s = 1.231 \times 10^{-3}$ and $k = 0.00282$ into the above formula, the LOD can be calculated as 2.16 μM.

Table S7. Comparisons of the FL detection for Fe^{3+} and PPi by using **1**-based sensor with some reported results.

Probe material	**Linear range of Fe^{3+}**	**LOD (μM)**	**Linear range of PPi**	**LOD (μM)**	**Ref.**
RBCB	10–100 μM	10.5	–	–	4
NCDs	5–60 μM	1.9	–	–	5
Eu-MOF	1–8 μM	2.31	–	–	6
DPYBT	3.8–7.2 μM	3.04	–	–	7
Zn^{2+}-Au/AgNCs	–	–	10–400 μM	3.2	8
Fe^{3+}-AuNCs@GSH	–	–	50–100 μM	28	9
Cu^{2+}-AuNCs	–	–	0–30 μM	2	10
Cu^{2+}-BCDs	–	–	25–500 μM	9.67	11
TA/Fe^{3+}–DCNPs	–	–	0–2 mM	3.36	12
N-CDs	5–40 μM	0.87	0–20 μM	0.66	13
carbon dots	0.5–400 μM	0.21	2–600 μM	0.86	14
PDA-GNPs	0.1–300 μM	0.03	2–12 μM	0.6	15
N-doped carbon quantum dots	0–600 μM	1.2	5–500 μM	0.5	16
N-CDs	3–30 μM	2.71	2–12 μM	1.12	17
1	0–150 μM	1.23	0–700 μM	2.16	This work

Table S8. Decay lifetimes of the Fe^{3+}-quenched system under different concentrations of PPi.

Concentration of PPi / μM	**τ_1 / μs**	**A_1**	**Percentage / %**	**τ_2 / μs**	**A_2**	**Percentage / %**	**τ**
100 μM	457.29	2041.85	100	/	/	/	457.29
200 μM	530.59	1946.98	100	/	/	/	530.59
300 μM	632.09	1876.98	100	/	/	/	632.09
400 μM	535.01	1209.37	54.92	832.75	637.69	45.08	669.22
500 μM	537.88	1284.86	52.72	922.56	671.77	47.28	719.75

600 μM	522.53	863.37	47.09	922.48	549.43	52.91	734.13
700 μM	633.45	1643.11	76.12	1330.42	245.45	23.88	799.90
800 μM	647.88	1697.36	76.72	1435.08	232.48	23.28	831.11

With the increase of PPi, the PL decay curves are more suitable to be fitted by second-order exponential function as $I = A_1exp(-t/\tau_1) + A_2exp(-t/\tau_2)$ (τ_1 and τ_2 are the fast and slow components of the luminescence lifetimes; A_1 and A_2 are the pre-exponential factors). The average lifetime is determined by the given formula $\tau = (A_1\tau_1^2 + A_2\tau_2^2)/(A_1\tau_1 + A_2\tau_2)$.[18]

Table S9. Decay lifetimes of the **1**-based sensor under different concentrations of PPi.

Concentration of PPi / μM	τ_1 / μs	A_1	Percentage / %	τ_2 / μs	A_2	Percentage / %	τ
100 μM	828.2	938.36	100	/	/	/	828.20
200 μM	831.77	959.92	100	/	/	/	831.77
300 μM	835.80	945.74	100	/	/	/	835.80
400 μM	840.21	992.66	100	/	/	/	840.21
500 μM	520.70	462.17	31.04	1000.00	534.62	68.96	851.22
600 μM	693.09	692.61	65.60	1233.65	204.06	34.40	879.05
700 μM	709.05	819.33	75.48	1491.04	126.60	24.52	900.83
800 μM	615.85	615.85	51.95	1189.31	313.55	48.05	891.41

With the increase of PPi, the PL decay curves are more suitable to be fitted by second-order exponential function as $I = A_1exp(-t/\tau_1) + A_2exp(-t/\tau_2)$ (τ_1 and τ_2 are the fast and slow components of the luminescence lifetimes; A_1 and A_2 are the pre-exponential factors). The average lifetime is determined by the given formula $\tau = (A_1\tau_1^2 + A_2\tau_2^2)/(A_1\tau_1 + A_2\tau_2)$.[18]

Table S10. Detection results of PPi in human serum sample by using Fe^{3+}-quenched system.

Sample	Spiked (μM)	Measure (μM)	Recovery (%)	RSD (n = 3, %)
Human serum	80	82.06	102.58	1.48
	160	159.51	99.69	0.73
	240	240.57	100.24	0.56

References

[1] J.-C. Liu, Q. Han, L.-J. Chen, J.-W. Zhao, C. Streb and Y.-F. Song, Aggregation of giant cerium–bismuth tungstate clusters into a 3D porous framework with high proton conductivity, *Angew. Chem. Int. Ed.*, 2018, **57**, 8416.

[2] M. V. Kirillova, C. I. M. Santos, V. André, T. A. Fernandes, S. S. P. Dias and A. M. Kirillov, Self-assembly generation, structural features, and oxidation catalytic properties of new aqua-soluble copper(II)-aminoalcohol derivatives, *Inorg. Chem. Front*., 2017, **4**, 968.

[3] X. Su, Y. Z. He, K. H. Li, M. Wang, W. Tang, S. H. Zhang, P. T. Ma, J. Y. Niu and J. P. Wang, Unleashing the power of directed electron transfer: unraveling the potential of $\{PV_4\}_2$ in heterogeneous photocatalysis, *Inorg. Chem.*

Front., 2024, **11**, 2965.

[4] P. S. Nayab and M. Shkir, Rapid and simultaneous detection of Cr (III) and Fe (III) ions by a new naked eye and fluorescent probe and its application in real samples, *Sens. Actuators B Chem*., 2017, **251**, 951.

[5] J. J. Cui, X. X. Zhu, Y. P. Liu, L. M. Liang, Y. S. Peng, S. G. Wu and Y. Zhao, N-doped carbon dots as fluorescent ''Turn-Off'' nanosensors for ascorbic acid and Fe^{3+} detection, *ACS Appl. Nano Mater.*, 2022, **5**, 7268.

[6] T.-Q. Lu, X.-T. Wang, L.-T. Cheng, C. Chen, H. Y. Shi, J. Zheng and X.-Y. Zheng, Soft metal−organic frameworks ased on $\{Na@Ln_6\}$ as a secondary building unit featuring a magnetocaloric effect and fluorescent sensing for cyclohexane and Fe^{3+}, *Cryst. Growth Des.,* 2021, **21**, 7065.

[7] J. N. Qian, N. Huang, Q. Y. Lu, C. Wen and J. B. Xia, A novel D-A-D-typed rod-like fluorescent material for efficient Fe(III) and Cr(VI) detection: Synthesis, structure and properties, *Sens. Actuators B Chem*., 2020, **320**, 128377.

[8] Z. L. Lei, J. Zhou, M. Liang, Y. Xiao and Z. H. Liu, Aggregation-induced emission of Au/Ag alloy nanoclusters for fluorescence detection of inorganic pyrophosphate and pyrophosphatase activity, *Front. Bioeng. Biotechnol*., 2021, **8**, 628181.

[9] P.-H. Li, J.-Y. Lin, C.-T. Chen, W.-R. Ciou, P.-H. Chan, L. Y. Luo, H.-Y. Hsu, E. W.-G. Diau and Y.-C. Chen, Using gold nanoclusters as selective luminescent probes for phosphate-containing metabolites, *Anal. Chem.,* 2012, **84**, 5484.

[10] Y. Chen, W. Y. Li, Y. Wang, X. D. Yang, J. Chen, Y. N. Jiang, C. Yu and Q. Lin, Cysteine-directed fluorescent gold nanoclusters for the sensing of pyrophosphate and alkaline phosphatase, *J. Mater. Chem. C*, 2014, **2**, 4080.

[11] Z.-X. Wang, X.-H. Yu, F. Li, F.-Y. Kong, W.-X. Lv, D.-H. Fan and W. Wang, Preparation of boron-doped carbon dots for fluorometric determination of Pb(II), Cu(II) and pyrophosphate ions, *Microchim. Acta*., 2017, **184**, 4775e4783.

[12] Y. Q. Su, L. Y. Ye, J. Y. Gu, L. Y. Zhao, Y. Y. Zhou and J. J. Peng, Sensing and imaging of PPi in vivo using lanthanide-based second near-infrared luminescent probes, *J. Mater. Chem. B*, 2022,**10**, 1055.

[13] A. Yu, Y. Tang, K. Li, J. Gao, Y. Zheng and Z. Zeng, Tunable photoluminescence studies based on blue-emissive carbon dots and sequential determination of Fe(III) and pyrophosphate ions, *Spectrochim. Acta Mol. Biomol. Spectrosc.,* 2019, **222**, 117231.

[14] Y. P. Hu, Z. J. Gao, J. Yang, H. Chen, L. Han, Environmentally benign conversion of waste polyethylene terephthalate to fluorescent carbon dots for ''on-off-on'' sensing of ferric and pyrophosphate ions, *J. Colloid Interface Sci*., 2019, **538**, 481.

[15] L. Tang, S. Mo, S. G. Liu, L. L. Liao, N. B. Li, H. Q. Luo, Synthesis of fluorescent polydopamine nanoparticles by Michael addition reaction as an analysis platform to detect iron ions and pyrophosphate efficiently and construction of an IMPLICATION logic gate, *Sens. Actuators B Chem*., 2018, **255**, 754.

[16] F. S. Niu, Y.-L. Ying, X. Hua, Y. S. Niu, Y. H. Xu and Y.-T. Long, Electrochemically generated green-fluorescent N-doped carbon quantum dots for facile monitoring alkaline phosphatase activity based on the Fe^{3+}-mediating ON-OFF-ON-OFF fluorescence principle, *Carbon*, 2018, **127**, 340.

[17] L. Y. Jin, X. S. Wang, X. Y. Liu, Y. L. Jiang and J. Shen, Preparation of novel fluorescent probe based on carbon

dots for sensing and imaging Fe(III) and pyrophosphate in cells and zebrafish, *Anal. and Bioanal. Chem.,* 2022, **414**, 7609.

[18] T. Fujii, K. Kodaira, O. Kawauchi, N. Tanaka, H. Yamashita and M. Anpo, Photochromic behavior in the fluorescence spectra of 9-anthrol encapsulated in Si−Al glasses prepared by the sol−gel method, *J. Phys. Chem. B,* 1997, **101**, 10631.